MDPI

Article

Numerical Study on Death of Squamous Cell Carcinoma Based on Various Shapes of Gold Nanoparticles Using Photothermal Therapy

Donghyuk Kim [ID] and Hyunjung Kim *[ID]

Department of Mechanical Engineering, Ajou University, Suwon-si 16499, Gyeonggi-do, Korea;
kimdonghyuk20@ajou.ac.kr
* Correspondence: hyunkim@ajou.ac.kr; Tel.: +82-31-219-2340

Abstract: Due to increased exposure to ultraviolet radiation caused by increased outdoor activities, the incidence of skin cancer is increasing. Incision is the most typical method for treating skin cancer, and various treatments that can minimize the risks of incision surgery are being investigated. Among them, photothermal therapy is garnering attention because it does not cause bleeding and affords rapid recovery. In photothermal therapy, tumor death is induced via temperature increase. In this study, a numerical study based on heat transfer theory was conducted to investigate the death of squamous cell carcinoma located in the skin layer based on various shapes of gold nanoparticles (AuNPs) used in photothermal therapy. The quantitative correlation between the conditions of various AuNPs and the laser intensity that yields the optimal photothermal treatment effect was derived using the effective apoptosis ratio. It was confirmed that optimal conditions exist for maximizing apoptosis within a tumor tissue and minimizing the thermal damage to surrounding normal tissues when using AuNPs under various conditions. Furthermore, it is envisioned that research result will be utilized as a standard for photothermal treatment in the future.

Keywords: apoptosis; continuous wave laser; gold nanoparticles; heat transfer; hyperthermia; numerical analysis; photothermal therapy; squamous cell carcinoma; thermal damage

1. Introduction

Recently, ultraviolet exposure has increased due to increased outdoor activities as a result of global economic development. Accordingly, the incidence of skin cancer is increasing annually [1,2]. Skin cancer can be primarily classified into squamous cell carcinoma, basal cell carcinoma, and malignant melanoma, and the treatment of these skin cancers is performed using various methods such as chemotherapy, cryotherapy, and incision [3–5]. These therapy methods, however, pose various negative effects [6–8]. In particular, surgery via incision causes bleeding and possible secondary infection [9,10].

An alternative treatment (i.e., photothermal therapy) is garnering attention as a method that can alleviate these adverse effects [11,12]. Photothermal therapy is a treatment method that uses the photothermal effect, a phenomenon in which light energy is converted into thermal energy when light energy is irradiated onto a medium, to induce the death of tumor tissues by increasing the temperature of the target tumor tissue [13,14]. This treatment method affords quick recovery and minimal risk of subsequent infection [15,16]. Photothermal therapy primarily supplies heat to biological tissues via laser, thereby affording the easy control of the heating range and intensity [17,18]. When a visible ray laser is used (among lasers of various wavelengths), a significant amount of light absorption occurs not only in the target tumor tissue, but also in normal tissues. Hence, laser in the near-infrared region, which involves a low light-absorption coefficient in biological tissues, is applied in photothermal therapy [19]. However, because the tumor tissue has a low light absorption rate with respect to laser in the near-infrared region, a light absorption enhancer is injected

into the tumor tissue to increase the light absorption rate of the tumor tissue to perform treatment. This causes a temperature increase in only the tumor tissue, enabling selective treatment [20]. Among the various light absorption enhancers, gold nanoparticles (AuNPs) are widely used because they are harmless to the human body and afford high surface workability [21–23]. AuNPs reach the tumor in various ways such as direct administration and intravenous injection, and are injected into the tumor through a process such as endocytosis and used for treatment [24–26].

Biological tissues including tumor tissues cause various types of death depending on temperature [27,28]. Apoptosis occurs between 43 °C and 50 °C, and is a form of self-death that does not affect the surroundings. Necrosis, in contrast, occurs at temperatures of 50 °C or above; it poses the risk of cancer cell metastasis and recurrence as it affects adjacent tissues when the tissue dies. Accordingly, the temperature range corresponding to apoptosis should be maintained to prevent necrosis. In photothermal therapy, treatment is performed by controlling the appropriate intensity of the heat source, injection amount of AuNPs, and type of AuNPs to minimize thermal damage to surrounding normal tissues while maintaining a temperature band corresponding to apoptosis [29].

Based on these factors, various studies regarding photothermal therapy are being conducted. Nam et al. [30] conducted an experimental study pertaining to photothermal therapy combined with chemotherapy. Polydopamine-coated spike-shaped AuNPs with excellent photothermal stability and optical efficiency were developed to enable photothermal therapy; consequently, successful treatment for 85% of CT26 colon carcinoma cases was confirmed. In addition, the therapeutic efficacy of TC-1 submucosa-lung metastasis was confirmed. Mackey et al. [31] conducted a study regarding photothermal therapy using rod-type AuNPs. The study was conducted both theoretically and in vitro, and information pertaining to the shapes of three sizes of gold nanorods that afforded the optimal therapeutic effect was obtained. Finally, it was demonstrated that gold nanorods with a length of 28 nm and a diameter of 8 nm were the most effective light absorption enhancers. Broek et al. [32] conducted an experimental study regarding photothermal therapy using branched AuNPs. In this study, branched AuNPs were biofunctionalized with nanobodies of heavy chain-only antibodies and bound to HER2 antigen expressed in both breast and ovarian cancer cells. As a result of the treatment, it was confirmed that the tumor died when 690 nm continuous wave (CW) laser was irradiated with an intensity of 38 W/cm^2 for 5 min, and that the tumor was killed only under an optical density of 4 or higher when the corresponding AuNP was used. Xi et al. [33] developed new photothermal agents (PTAs) to improve the low photothermal conversion efficiency (PCE) of conventional PTAs. PCE is facilitated by the -CF3 moiety included in the meso-position of the BODIPY scaffold in the PTAs because the free rotation of -CF3 provides a pathway for efficient non-radiative decay. In addition, it was confirmed that the barrier-free rotation of -CF3 continued even when tfm-BDP was encapsulated with polymer nanoparticles. Excellent therapeutic effects were confirmed in both in vitro and in vivo experiments, and mouse experiments confirmed that tfm-BDPNP was efficiently accumulated in the tumor area and completely resected tumor tissue when near-infrared lasers of 0.3 W/cm^2, 808 nm were used.

In summary, studies regarding photothermal therapy under various conditions have been conducted both experimentally and theoretically. However, treatment trends based on different types of AuNPs and laser irradiation conditions could not be determined, and studies suggesting optimal treatment conditions quantitatively when considering various AuNP concentrations and other conditions at the same time are insufficient. In addition, although photothermal therapy induces cell death through temperature increase due to the photothermal effect, studies pertaining to heat transfer are insufficient. Therefore, in this study, a numerical study of photothermal therapy based on heat transfer theory was conducted for actual skin layers including squamous cell carcinoma. The temperature distribution in tumor and normal tissues based on various AuNPs shapes, laser intensities, and volume fractions of injected AuNPs was obtained. In addition, the optimal treatment effect was proposed by quantitatively confirming conditions that maximize the apoptosis

of tumor tissues while minimizing thermal damage to surrounding normal tissues, which is the main purpose of photothermal therapy based on the apoptotic variable proposed by Kim et al. [34].

2. Materials and Methods

2.1. Discrete Dipole Approximation (DDA) Method

In this study, the DDA method [35,36] was used to calculate the optical efficiency of various nanoparticles. In this method, the scattering and absorption characteristics are calculated after assuming that dipoles with polarized shapes are formed at regular intervals based on information regarding a specific shape. Compared with the Mie theory [37,38], which can be applied only to existing spheres or ellipses, the DDA method allows a wide range of shapes that can be calculated and applied. In addition, compared to the finite difference domain method, the DDA method has the advantage of being very fast in computation speed and requiring less memory for computation [39].

To perform calculations using the DDA method, the polarization vector P must be determined. P depends on the interaction between the dipole and local electric field E; it can be calculated using Equation (1), where α is the polarizability, and r is the position vector. In addition, the local electric field E can be calculated using Equation (2).

$$P_i = \alpha_i \cdot E_i(r_i) \tag{1}$$

$$E_i(r_i) = E_{inc,i} - \sum_{j \neq i}^{N} A_{ij} \cdot P_j \ \ (i,j = 1,2,3,\ldots,N) \tag{2}$$

$$E_{inc,i} = E_0 e^{i(k \cdot r_i)} \tag{3}$$

$$A_{ij} \cdot P_j = \frac{e^{i(k \cdot r_{ij})}}{r_{ij}^3} \left\{ k^2 r_{ij} \times (r_{ij} \times P_j) + \frac{1 - ikr_{ij}}{r_{ij}^2} \times \left[k^2 P_j - 3r_{ij}(r_{ij} \cdot P_j) \right] \right\} \ (i \neq j) \tag{4}$$

where k is the wavenumber of the radiation. The electric field at position i due to the dipole at position j is included in the second term on the right side of Equation (2). Meanwhile, A is the interaction matrix between the dipoles (Equation (4)), where r_{ij} is $|r_i - r_j|$, and A_{ij} is the interaction matrix under the condition that $i \neq j$. If i and j are the same, then the interaction matrix can be simplified as α_i^{-1}. Subsequently, Equation (2) can be transformed into a three-dimensional complex linear equation; hence, the P of each dipole can be calculated.

In the case of the absorption, attenuation, and scattering, cross-sections can be calculated as shown in Equations (5)–(7) using the calculated P, where * denotes complex conjugation.

$$C_{abs} = \frac{4\pi k}{|E_0|^2} \sum_{i=1}^{N} \left\{ \text{Im} \left[P_i \cdot \left(\alpha_i^{-1} \right)^* P_i^* \right] - \frac{2}{3} k^3 P_i P_i^* \right\} \tag{5}$$

$$C_{ext} = \frac{4\pi k}{|E_0|^2} \sum_{i=1}^{N} \text{Im} \left(E_{inc,i}^* \cdot P_i \right) \tag{6}$$

$$C_{sca} = C_{ext} - C_{abs} \tag{7}$$

Finally, the absorption, attenuation, and scattering efficiencies can be calculated using Equation (8), where r_{eff} is the effective radius of the particle, and V is the volume of the particle.

$$Q_{abs} = \frac{C_{abs}}{\pi r_{eff}^2}, \ \ Q_{ext} = \frac{C_{ext}}{\pi r_{eff}^2}, \ \ Q_{sca} = \frac{C_{sca}}{\pi r_{eff}^2} \tag{8}$$

$$r_{eff} = \left(\frac{3V}{4\pi} \right)^{(1/3)} \tag{9}$$

2.2. Heat Transfer Model and Optical Properties

In this study, the Pennes bioheat equation [40], which is widely used in the field of bio-heat transfer, was used for the thermal analysis of biological tissues. In this equation, it is assumed that the heat generated by blood and metabolism is uniformly generated in the biological tissue, as expressed in Equation (10).

$$\rho c_p \frac{\partial T}{\partial t} = k_m \nabla^2 T + q_b + q_{met}, \tag{10}$$

where ρ is the density; c_p is the specific heat; T is the temperature; and k_m is the thermal conductivity of the medium. q_b and q_{met} are the heat generated by blood flow and metabolism, respectively. In this study, the skin surface was irradiated with a Gaussian profile laser, and the temperature was increased via the photothermal effect. Therefore, the heat generated by the laser must be simultaneously considered [41]. In addition, the heat generated by metabolism and the blood flow is insignificant compared with the heat generated by the laser, and Equation (10) is written as shown in Equation (11) to confirm the study results under steady-state conditions.

$$- k_m \nabla^2 T = q_l \tag{11}$$

$$q_l = \mu_{abs} \frac{P_l}{\pi r_l} e^{-\mu_{tot} z} \cdot e^{-\frac{r^2}{r_l^2}} \quad (\mu_{tot} = \mu_{abs} + \mu'_{sca}), \tag{12}$$

where μ_{abs} is the light absorption coefficient of the medium; P_l is the laser intensity; and r_l is the laser radius. μ_{tot} represents the total light attenuation coefficient of the medium and is the sum of the absorption coefficient (μ_{abs}) and attenuated scattering coefficient (μ'_{sca}) of the medium.

The optical properties of the medium should be calculated separately for normal and tumor tissues. For the former, because AuNPs are not injected into them, only their optical properties are considered. However, for the tumor tissues, because various shapes of AuNPs are injected inside them, the corresponding optical properties must be considered simultaneously.

$$\mu_{abs,n} = 0.75 f_v \frac{Q_{abs,n}}{r_{eff}}, \quad \mu_{sca,n} = 0.75 f_v \frac{Q_{sca,n}}{r_{eff}} \tag{13}$$

$$\mu'_{sca,n} = \mu_{sca,n}(1 - g) \tag{14}$$

$$\mu_{abs} = \mu_{abs,n} + \mu_{abs,m}, \quad \mu'_{sca} = \mu'_{sca,n} + \mu'_{sca,m} \tag{15}$$

Equations (13)–(14) are equations that represent the optical properties of AuNPs [42], where f_v is the volume fraction of AuNPs in the tumor; g is the anisotropy coefficient; and Q_{abs} and Q_{sca} are the absorption and scattering efficiencies of the particles, respectively. Finally, the optical properties of the medium containing AuNPs were calculated as the sum of the optical properties of the AuNPs and the medium, as shown in Equation (15). The optical property of the medium is not a calculated value, but an intrinsic property of the material. The optical efficiency of AuNPs was calculated using the DDA method described above, and it was assumed that the injected AuNPs were uniformly distributed in the medium [43].

2.3. Apoptotic Variables

In this study, three variables proposed by Kim et al. [34] were used to quantitatively confirm the therapeutic effect of photothermal treatment.

First, the apoptosis ratio (θ_A), which represents the quantity of tumor tissues that undergo apoptosis at a temperature range of 43 °C–50 °C, was calculated as the ratio of the volume of the tumor tissue to the tissue volume entering the temperature band

corresponding to apoptosis. For example, if all regions of the tumor are in the temperature band of apoptosis, then θ_A is 1.

$$\theta_A = \frac{apoptosis\ volume\ (if\ 43 < V(T) < 50)}{tumor\ volume} \tag{16}$$

$$\theta_H = \frac{\sum_{i=1}^{n}(V_i(T) \cdot w_i)}{V_i} \tag{17}$$

Next, the thermal hazard value (θ_H), which quantitatively represents the amount of thermal damage to normal tissues, is the ratio between the normal tissue volume and weighted sum that affects each phenomenon based on the temperature of the biological tissue, as shown in Equation (17). The phenomena that occur in each temperature range in the biological tissue are shown in Table 1 [44,45]. The minimum value of θ_H was 1, indicating that all regions of the normal tissue corresponded to 37 °C to 43 °C.

Table 1. Laser-induced thermal effects [44,45].

Temperature Range (°C)	Biological Effect	Weight, w
37	Normal	1
$37 < T < 43$	Biostimulation	1
$43 \leq T < 45$	Hyperthermia	2
$45 \leq T < 50$	Reduction in enzyme activity	2
$50 \leq T < 70$	Protein denaturation (coagulation)	3
$70 \leq T < 80$	Welding	4
$80 \leq T < 100$	Permeabilization of cell membranes	5
$100 \leq T < 150$	Vaporization	6

As shown in Equation (17), the result for θ_H varies depending on the range of normal tissues for calculating thermal damage. Accordingly, in this study, the range of the normal tissue surrounding the tumor tissue was selected as 50% of the length of the tumor tissue.

Finally, the effective apoptosis ratio (θ_{eff}), which quantitatively represents the maximal occurrence of apoptosis in tumor tissues and the minimal occurrence of thermal damage to surrounding normal tissues simultaneously (i.e., the ultimate purpose of photothermal therapy), is the ratio between θ_A and θ_H, as shown in Equation (18). Because θ_{eff} is the relative value between the ratio of the volume corresponding to the temperature band where apoptosis occurs in the tumor tissue and the amount of thermal damage to the surrounding normal tissues, more effective treatment is induced as θ_{eff} increases. Finally, the optimal conditions for photothermal therapy can be determined using θ_{eff}.

$$\theta_{eff} = \frac{apoptosis\ ratio(\theta_A)}{thermal\ hazard\ value(\theta_H)} \tag{18}$$

2.4. Validation of Numerical Model

To verify the numerical analysis model to be used in this study, the studies of Soni et al. [46] and Ren et al. [47] were used. The study assumed that a cylindrical tumor was located from the surface in cylindrical normal tissues as shown in Figure 1, and assumed that AuNPs in the tumor were uniformly distributed. Normal tissue has a radius of 20 mm and a depth of 10 mm, and a tumor tissue has a radius of 10 mm and a depth of 5 mm. The radius of the irradiated laser was selected to be 10 mm, which is the same as the radius of the tumor, and the intensity of the laser was 0.5 W/cm^2. In addition, convection with air exists at the skin surface, and the initial temperature of all media was assumed to be 37 °C. The thermal and optical properties of normal and tumor tissues are summarized in Table 2.
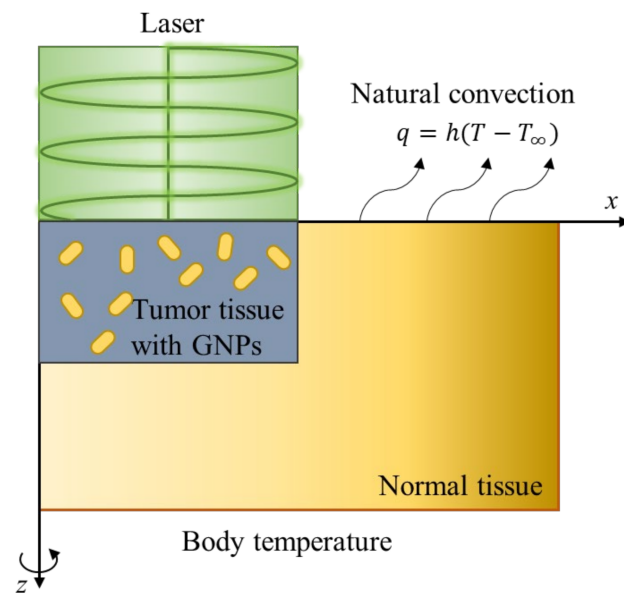
Figure 1. Schematic figure of the validation numerical model.

Table 2. Thermal and optical properties used in the validation numerical analysis model.

	Tumor Tissue & AuNPs	Normal Tissue
Absorption coefficient (cm^{-1})	121	0.02
Reduced scattering coefficient (cm^{-1})	0.5	6.5
Density (kg/m^3)	1100	1000
Specific heat (J/kgK)	4200	4200
Thermal conductivity (W/mK)	0.55	0.5

Figure 2 is a graph of the validation results with the numerical analysis model in this study. The temperature along the radial direction when the depth was 0 mm and 5 mm in the central part of the tumor was confirmed, and the error was within about 1.4%. Through this, it was confirmed that the numerical analysis model used in this study was valid.
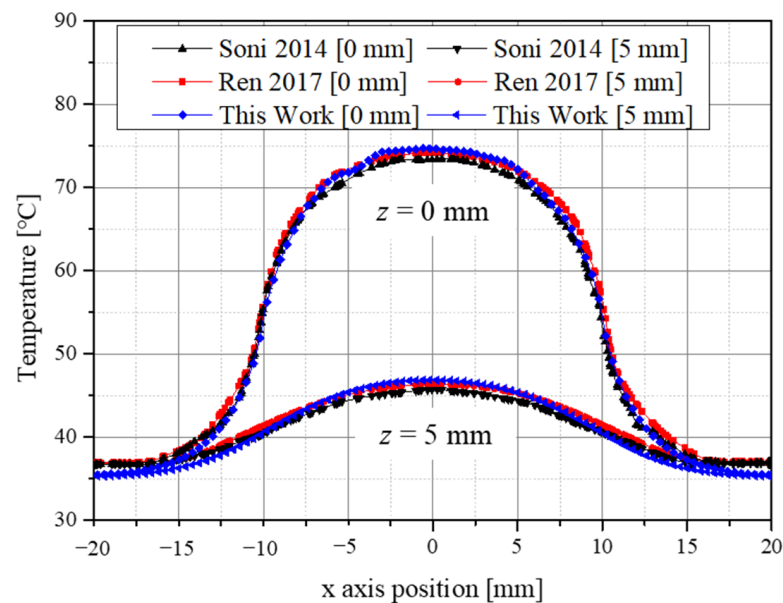

Figure 2. Validation result of the numerical model.

2.5. Numerical Investigation

In this study, a numerical analysis of photothermal therapy was conducted on a skin structure composed of four layers that included squamous cell carcinoma, as shown in Figure 3. The radius and depth of the entire normal tissue were 10 and 6 mm, respectively. It was assumed that tumor tissues with a radius of 5 mm and a depth of 2 mm were present on the skin surface. In addition, the irradiated laser exhibited a Gaussian distribution and had the same radius of 5 mm as the tumor tissue. The thickness of each skin layer and the thermal properties of all the media are summarized in Table 3. For the optical properties of the tumor and skin layer, the studies of Meglinski et al. [19] and Salomatina et al. [48] were referenced since values at various wavelengths were required.
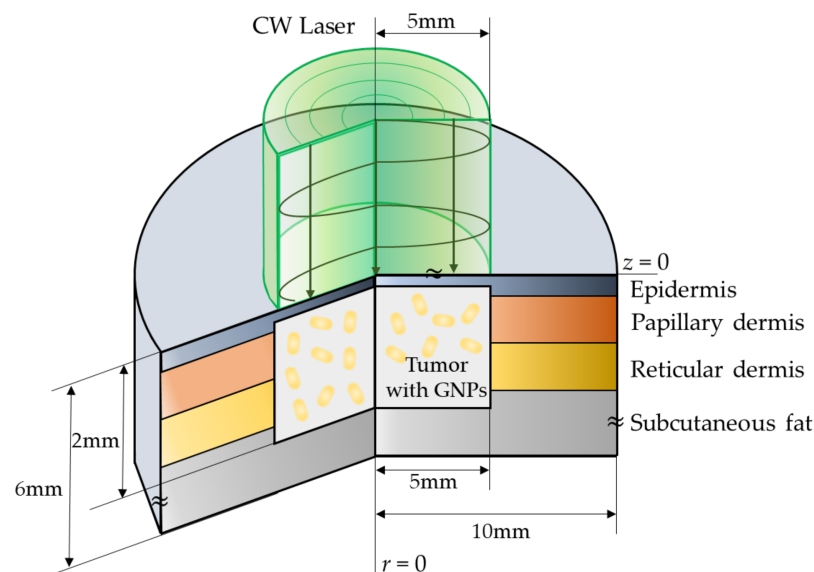

Figure 3. Schematic illustration of the numerical model.

Table 3. Thermal properties of the skin layer and tumor [49–54].

	d (mm)	ρ (kg/m^3)	c_p(J/kgK)	k (W/mK)
Epidermis	0.08	1200	3589	0.235
Papillary dermis	0.5	1200	3300	0.445
Reticular dermis	0.6	1200	3300	0.445
Subcutaneous fat	4.82	1000	2500	0.19
Tumor tissue	2	1070	3421	0.495

Using the numerical analysis model, the thermal behavior of tumor tissues and the surrounding normal tissues for various laser intensities, volume fractions of injected AuNPs, and AuNP types were confirmed, and the conditions are shown in Table 4. The laser intensity was set from 0 to 1.2 W with 0.002 W intervals. Meanwhile, six types of AuNPs with diameters ranging from 10 to 50 nm were selected at intervals of 5 nm, and the volume fraction of injected AuNPs in the tumor was classified into four stages from 10^{-3} to 10^{-6}.

Table 4. Conditions used in the numerical analysis.

Numerical Parameter	Case	Number	Remarks
Laser power (P_l)	0 to 1.2 W	601	Interval: 0.002 W
Type of AuNP	Rod, sphere, shell, pyramid, prism, cube	6	
Size of AuNP (r_{eff})	10 to 50 nm	9	Interval: 5 nm
Volume fraction of AuNP (f_v)	10^{-3} to 10^{-6}	4	Interval: 10^{-1}

As described above, six AuNPs were injected into the tumor, as shown in Figure 4. In the rod-type AuNPs, the aspect ratio was fixed at 6.67; in the shell-type AuNPs, the

difference between the outer diameter and the inner diameter was fixed at 4 nm; and in the prism-type AuNPs, the aspect ratio was fixed at 1.67. Finally, for various shapes of AuNPs, their absorption and scattering efficiencies were calculated in the wavelength range of 500 to 1500 nm using the DDA method.
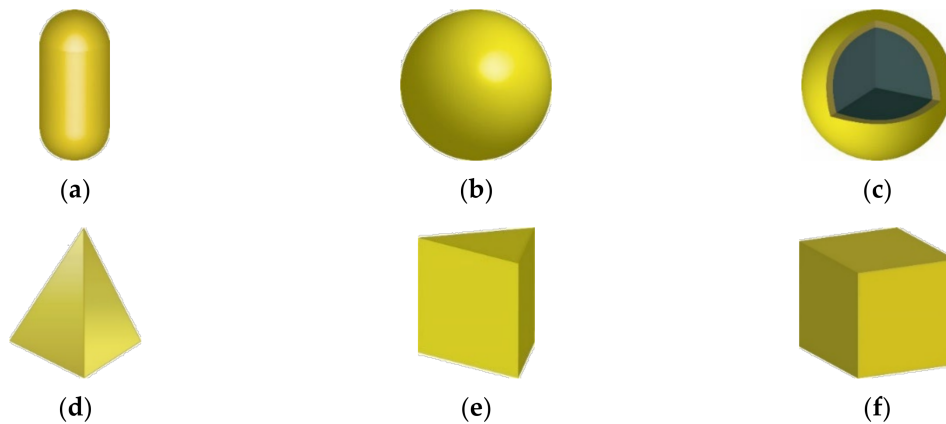

(**a**)　　　　　　　　　　　　(**b**)　　　　　　　　　　　　(**c**)

(**d**)　　　　　　　　　　　　(**e**)　　　　　　　　　　　　(**f**)

Figure 4. Various types of gold nanoparticles: (**a**) rod type; (**b**) sphere type; (**c**) shell type; (**d**) pyramid type; (**e**) prism type; and (**f**) cube type.

Finally, a numerical analysis of photothermal treatment was performed on the skin layer containing squamous cell carcinoma under the various conditions described above. For all cases, the temperature distribution of tumor tissues and the surrounding normal tissues was obtained, and the optimal treatment conditions were derived to maximize the temperature band corresponding to the apoptosis of tumor tissues while minimizing thermal damage to the surrounding normal tissues.

3. Results

3.1. Derivation of Optical Properties for Various AuNP Types

The optical efficiencies of AuNPs with various shapes were calculated using the DDA method. Figure 5 shows the absorption efficiency and scattering efficiency of the rod-type AuNPs. Calculations were performed for a wavelength range of 500 to 1500 nm, and it was confirmed that a laser wavelength that results in the optimal efficiency exists for each r_{eff}.
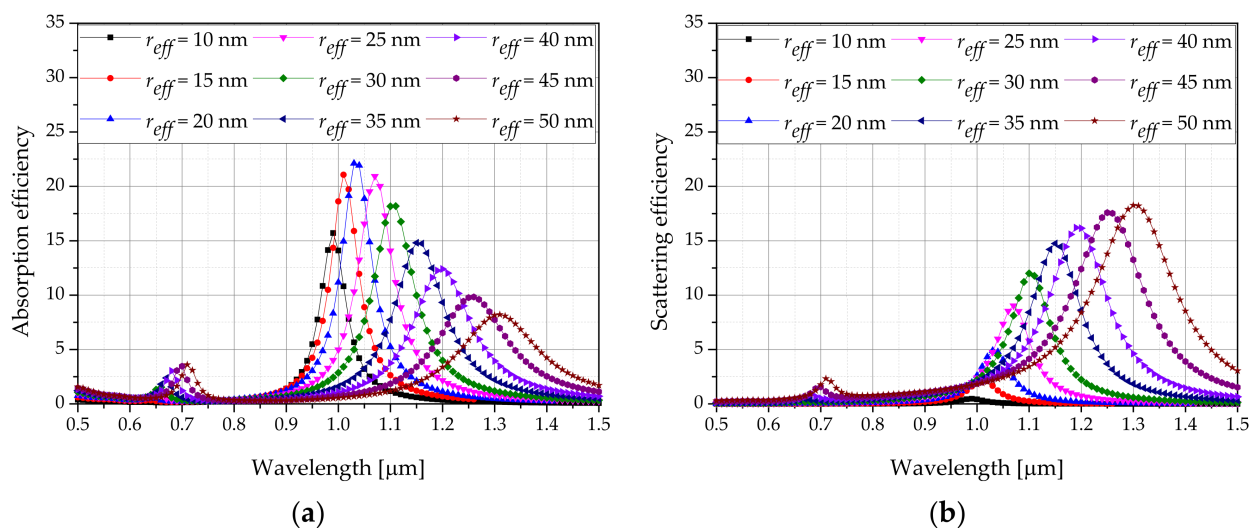

(**a**)　　　　　　　　　　　　　　　　　　　　　(**b**)

Figure 5. Optical efficiency of gold nanorods for various wavelengths: (**a**) absorption efficiency; (**b**) scattering efficiency.

Analysis was performed on AuNPs of six different shapes, and the wavelength (λ_{max}) values with the maximum absorption efficiency at various shapes and r_{eff} were recorded. The absorption and scattering efficiencies at the corresponding wavelengths are summarized in Table 5. In the case of r_{eff}, after the size of the particles is determined, it is calculated through Equation (9), and the size of the particles having a value as close as possible to the r_{eff} range presented in this study was set. As shown in Table 5, the absorption efficiency of the rod type was generally greater than that of the other types of AuNPs. In addition, the absorbance efficiency increased with r_{eff} increased generally. However, for the rod and shell types, the r_{eff} with the optimal absorbance efficiency existed depending on r_{eff}. Finally, the temperature distribution inside the tumor and normal tissues when the volume fraction of AuNPs was changed to achieve the optimal optical efficiency conditions based on the shape of various AuNPs was obtained.

Table 5. Derivation of optical efficiency for AuNPs of various shapes.

AuNP Type	r_{eff}(nm)	λ_{max}(nm)	Q_{abs}	Q_{sca}
Rod	10.01	990	15.7160	0.4703
	15.58	1010	21.0660	2.2822
	20.02	1030	22.1100	4.9106
	25.58	1070	20.9410	9.0330
	30.02	1110	18.1880	11.7830
	35.59	1150	14.8070	14.7490
	40.03	1200	12.4000	16.1530
	45.60	1260	9.8333	17.5270
	50.04	1310	8.2106	18.2100
Sphere	10	510	0.4589	0.0016
	15	510	0.7113	0.0082
	20	510	0.9880	0.0266
	25	510	1.2914	0.0669
	30	510	1.6168	0.1424
	35	510	1.9491	0.2676
	40	510	2.2594	0.4531
	45	520	2.5419	0.8789
	50	520	2.7331	1.2601
Shell	9.96	530	1.1211	0.0040
	15.16	560	2.8056	0.0476
	20.11	590	5.6807	0.2735
	24.97	630	8.9640	1.0629
	30.03	650	8.6687	1.5817
	35.09	630	9.3365	2.5683
	39.99	860	8.4822	1.6203
	44.95	720	8.2782	1.7524
	49.98	720	7.1150	1.3602
Pyramid	10.04	590	1.3073	0.0044
	15.06	590	2.0064	0.0228
	20.07	600	2.7377	0.0804
	24.94	600	3.4829	0.1943
	29.96	610	4.1738	0.4310
	34.98	620	4.7951	0.8355
	40.15	630	5.2890	1.4857
	45.01	640	5.4828	2.3042
	49.88	650	5.3941	3.2793
Prism	10.02	530	0.6632	0.0017
	15.02	530	1.0137	0.0086
	20.03	530	1.3802	0.0268
	25.04	530	1.7562	0.0639
	30.05	540	2.1391	0.1424
	35.06	540	2.5227	0.2510
	40.06	540	2.8719	0.3962
	45.07	550	3.1703	0.6303
	50.08	550	3.4553	0.8469
Cube	9.93	530	0.8433	0.0031
	14.89	530	1.3110	0.0163
	19.85	530	1.8217	0.0532
	25.12	530	2.4007	0.1401
	30.09	530	2.9437	0.2905
	35.05	530	3.4159	0.5221
	40.01	540	3.8570	1.0409
	44.98	540	4.0785	1.5180
	49.94	540	4.0361	1.9763

3.2. Temperature of Tumor and Normal Tissues for Various Conditions

　　　Figure 6 shows the temperature distribution of the normal and tumor tissues when the laser intensity was 0.4 W and the volume fraction of injected AuNPs was 10^{-3} and 10^{-6}, separately. The injected AuNPs were of the rod type—their aspect ratio and r_{eff} were 6.67 and 50 nm, respectively. When the volume fraction of AuNPs in the tumor was high ($f_v = 10^{-3}$), the light absorption coefficient of the tumor tissue including AuNPs was high. Therefore, a significant amount of laser energy was absorbed from the medium. Accordingly, the temperature of the tumor region increased significantly, as shown in Figure 6a. In addition, the temperature of the surrounding normal tissue increased because of heat conduction from the tumor tissue. In contrast, when the volume fraction of AuNPs in the tumor was low ($f_v = 10^{-6}$), the light absorption coefficient of the tumor tissue was low; therefore, even when a laser of the same intensity was used, the increase in temperature was insignificant, as shown in Figure 6b. The results confirmed that the temperature distribution of the tumor and surrounding normal tissues differed depending on the volume fraction of AuNPs in the tumor. Therefore, in this study, by obtaining the temperature distribution in the medium based on various shapes and volume fractions of AuNPs, the degree of thermal damage to the surrounding normal tissue as well as the corresponding temperature range that caused apoptosis were quantitatively confirmed.

3.3. Apoptosis Ratio

　　　In photothermal therapy, laser is irradiated to the affected area to kill the tumor tissue by increasing the temperature via the photothermal effect. From a temperature perspective, the temperature band corresponding to apoptosis must be maintained to prevent necrosis; therefore, the extent to which the apoptosis temperature band is maintained must be determined quantitatively by verifying the temperature distribution in the tumor tissue.

　　　Figure 7 shows a graph of the apoptosis ratio (θ_A) as functions of P_l and f_v for the rod-type AuNPs with various r_{eff}. As shown in the graph, as r_{eff} increased, the intensity of the laser with the maximum θ_A increased. This is because, when calculating the absorption coefficient, as Q_a does not increase at the same rate as r_{eff}, the absorption coefficient decreases, and a higher laser intensity is required to achieve the corresponding temperature range in which apoptosis occurs. In addition, it was confirmed that as f_v decreased, the intensity of the laser with the maximum θ_A increased. This is because as f_v decreased, the light absorption coefficient of the medium decreased; as such, the amount of heat absorbed by the medium decreased. Hence, the amount of heat generated by the laser must be increased to achieve the temperature band in which apoptosis occurs. Based on Figure 5, the condition in which the apoptosis ratio becomes 1 for all cases can be obtained.
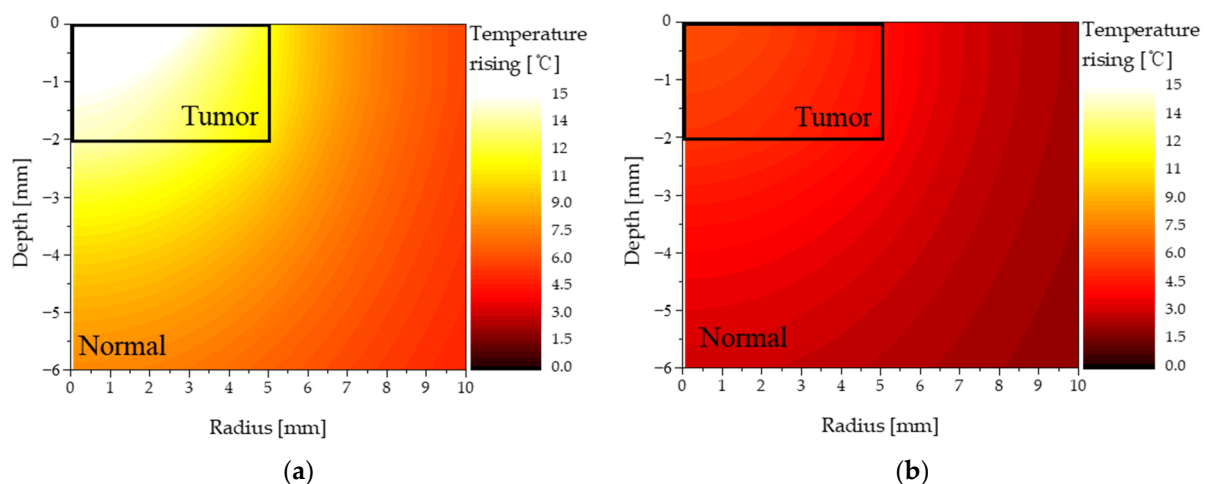

Figure 6. Temperature distribution of normal and tumor tissue (injected AuNPs: rod type): (**a**) $f_v = 10^{-3}$; (**b**) $f_v = 10^{-6}$.
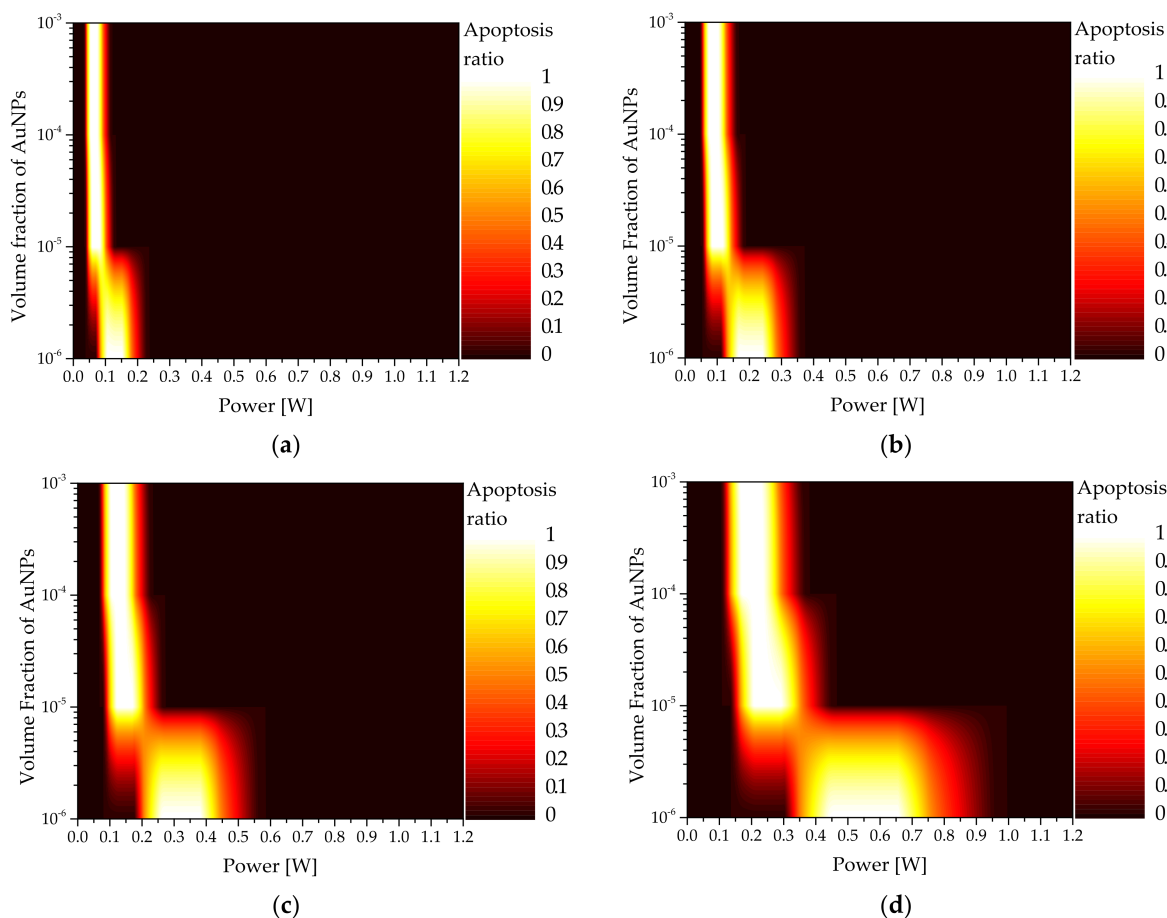
Figure 7. Apoptosis ratio (θ_A) for various volume fractions of AuNPs (f_v) (injected AuNPs: rod type) (**a**) r_{eff} = 10 nm; (**b**) r_{eff} = 25 nm; (**c**) r_{eff} = 35 nm; (**d**) r_{eff} = 50 nm.

3.4. Thermal Hazard Value

One of the most significant goals of photothermal therapy is to maintain a temperature range of 43 °C–50 °C in the tumor, which is known to cause apoptosis. Although direct heating using laser is not performed to the surrounding normal tissues, temperature increase is inevitable due to conduction heat transfer from the tumor tissue. Hence, the death of surrounding normal tissues due to temperature increase must be minimized by verifying the temperature distribution of not only the tumor tissue, but also the surrounding normal tissues. Accordingly, in this study, the amount of thermal damage to the surrounding normal tissues was quantitatively confirmed based on the thermal hazard value (θ_H) (Equation (17)).

Figure 8 shows θ_H as functions of P_l and f_v for sphere-type AuNPs with various r_{eff}. As shown in the graphs, as f_v increased, θ_H at the same P_l was high. This is because when f_v increased, the light absorption coefficient of the medium increased and the amount of heat absorbed by the tumor tissue increased; therefore, the temperature of the surrounding normal tissue increased higher, and the amount of thermal damage increased. Meanwhile, as r_{eff} increased, θ_H decreased. This is because as r_{eff} increased, the light absorption coefficient of the medium decreased, as described in Section 3.3, which implies that the amount of heat absorbed by the medium decreased at the same laser intensity, and the temperature increased slowly.
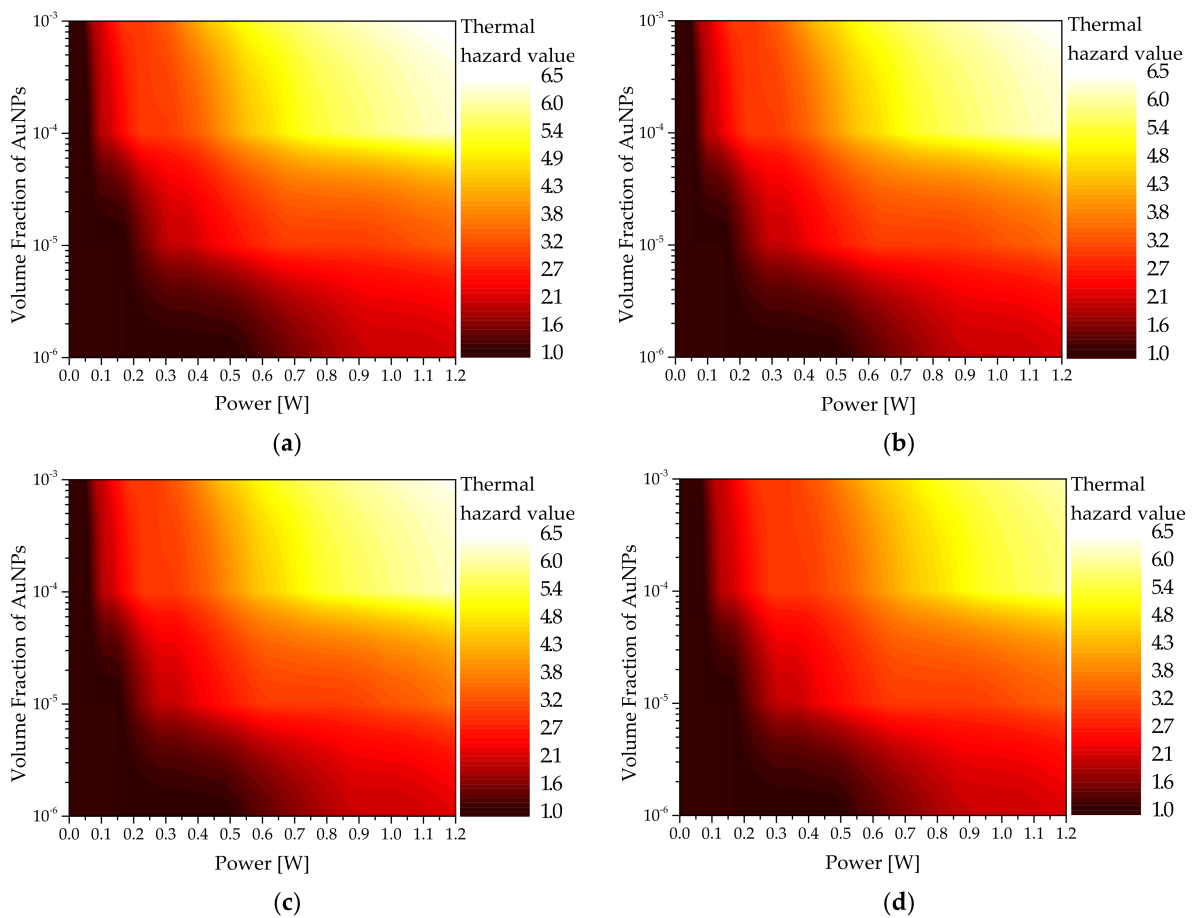
Figure 8. Thermal hazard value (θ_H) for various volume fractions of AuNPs (f_v) (injected AuNPs: sphere type): (**a**) r_{eff} = 10 nm; (**b**) r_{eff} = 25 nm; (**c**) r_{eff} = 35 nm; (**d**) r_{eff} = 50 nm.

3.5. Effective Apoptosis Ratio

Previously, the apoptosis ratio (θ_A) and thermal hazard value (θ_H) were used to define the conditions for maximizing the temperature range where apoptosis occurs in the tumor tissue and the relative ratio of thermal damage amount to the surrounding normal tissue. To confirm the distribution of the effective apoptosis ratio (θ_{eff}), which combines the two variables above, calculations were performed based on the shape and size of the AuNPs as well as the volume fraction of the injected AuNPs.

Figure 9 shows θ_{eff} as functions of P_l and f_v for shell-type AuNPs with various r_{eff}. As shown, the P_l value that results in the maximum θ_{eff} existed for each f_v, and that the P_l with the maximum θ_{eff} decreased as f_v increased. This is because, as described above, when f_v increased, the light absorption coefficient of the medium increased and the amount of heat absorbed from the medium increased; therefore, the intensity of the laser required to maintain the temperature range where apoptosis occurs was decreased.

In addition, as r_{eff} increased, the intensity of the laser at which θ_{eff} was maximized increased. However, for the shell-type AuNPs, as shown in Figure 9, the intensity of the laser that afforded the optimal treatment effect was not constant because r_{eff}, which maximized the absorption efficiency for various r_{eff}, existed. In addition, it was confirmed that an excessive increase in the laser intensity decreased θ_{eff} due to the increase in θ_H. The results confirmed that certain values of laser intensity and volume fraction of injected AuNPs yielded the optimal therapeutic effect for the different shapes and sizes of AuNPs. Figure 8 shows the derivation results of θ_{eff} for each r_{eff} for six types of AuNPs investigated in this study.
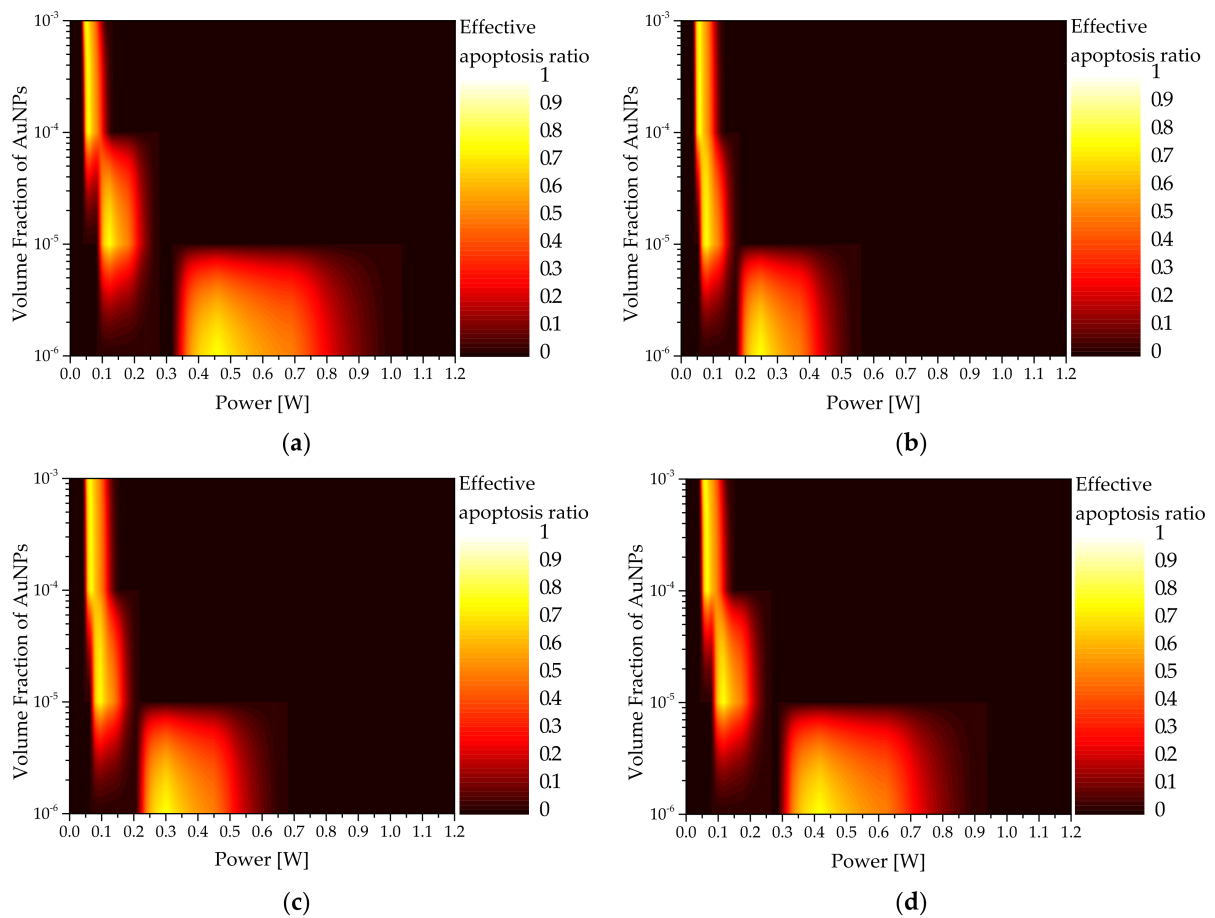
Figure 9. Effective apoptosis ratio (θ_{eff}) for various volume fractions of AuNPs (f_v) (injected AuNPs: shell type): (**a**) r_{eff} = 10 nm; (**b**) r_{eff} = 25 nm; (**c**) r_{eff} = 35 nm; (**d**) r_{eff} = 50 nm.

Based on the analysis, the volume fraction of injected AuNPs that resulted in the optimal therapeutic effect for all AuNP shapes was derived based on $f_v = 10^{-6}$. As shown in Figure 10, the optimal values of r_{eff} and P_l afforded the optimal therapeutic effect for various AuNP shapes. For the rod type, the absorption coefficient decreased as r_{eff} increased; consequently, P_l increased, and the optimal θ_{eff} was obtained. For the shell type, it was confirmed that the P_l value that afforded the optimal therapeutic effect was minimized as the absorption coefficient was maximized when r_{eff} was 25 nm.
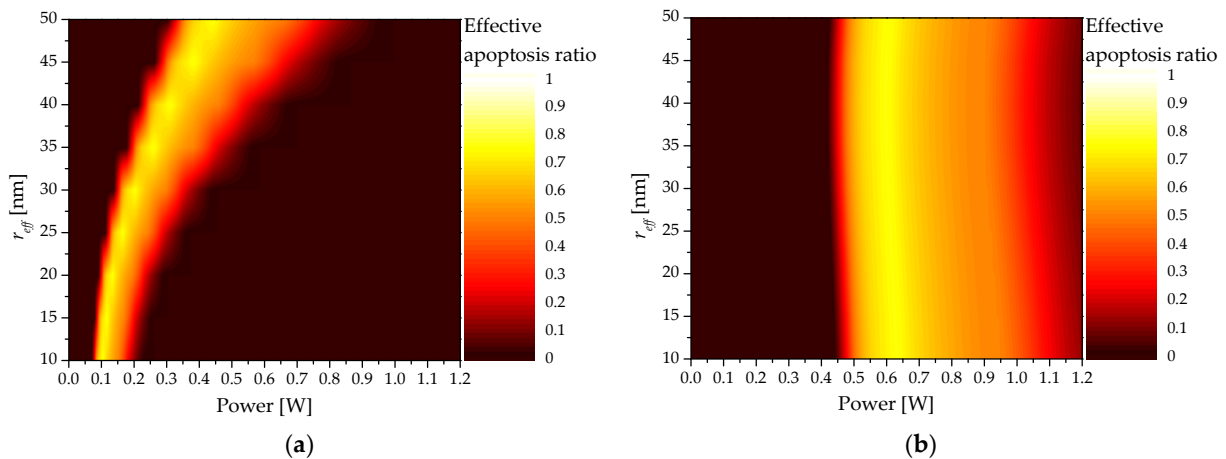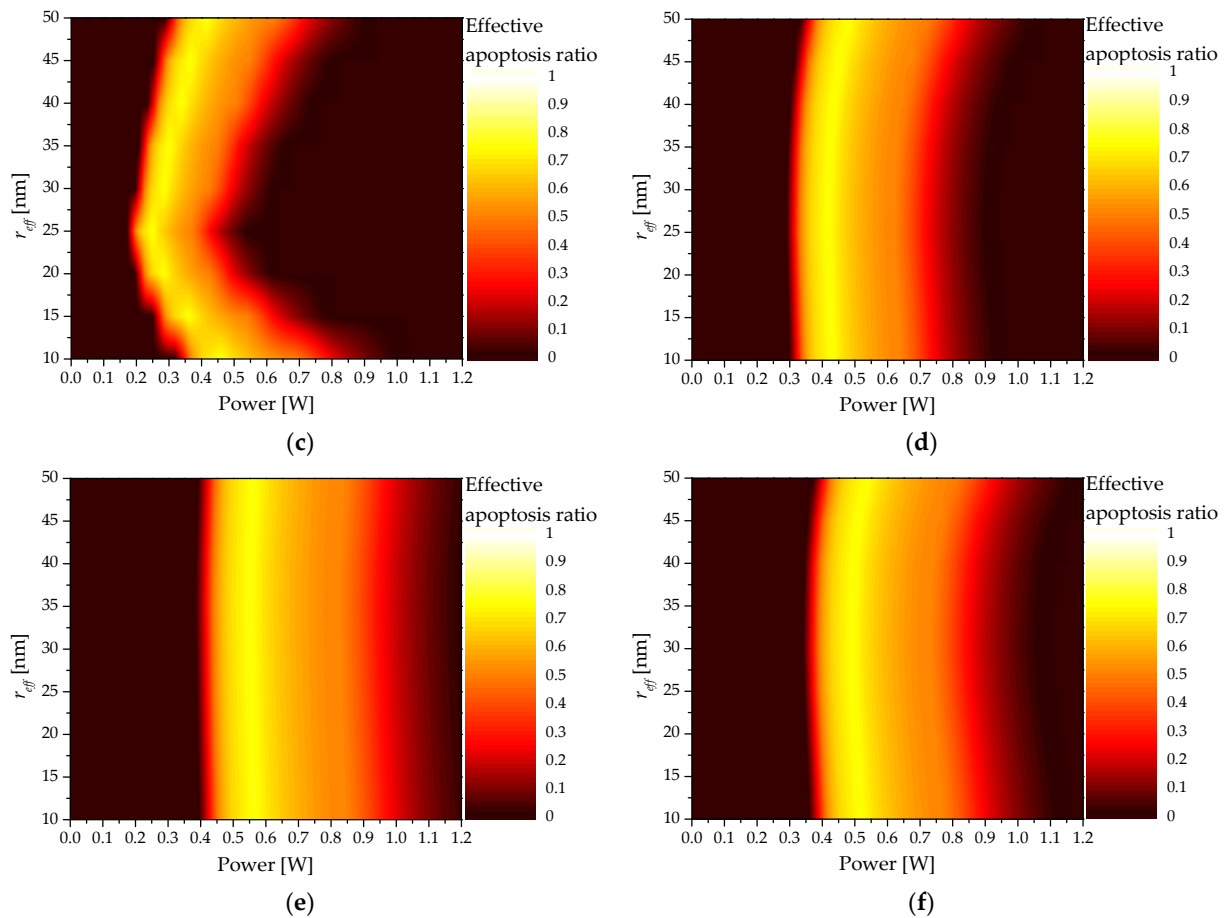

Figure 10. *Cont*.

Figure 10. Effective apoptosis ratio (θ_{eff}) for various types of AuNPs: (**a**) rod type; (**b**) sphere type; (**c**) shell type; (**d**) pyramid type; (**e**) prism type; (**f**) cube type.

For the pyramid and cube types, as r_{eff} increased, the absorption coefficient exhibited similar values; however, when r_{eff} was 40 nm, the absorption coefficient decreased and the optimal point of P_l decreased. For the sphere and prism types, the calculated absorption coefficients were similar as r_{eff} increased; as such, the optimum points of P_l based on r_{eff} were similar. Table 6 summarizes the f_v and P_l values that afforded the maximum θ_{eff} based on the shape and size of each AuNP.

Table 6. Optimal treatment conditions for various AuNP types and sizes.

AuNP Type	r_{eff}(nm)	λ_{max}(nm)	f_v	P_l(W)	Effective Apoptosis Ratio
	10.01	990	10^{-6}	0.104	0.74876
	15.58	1010	10^{-6}	0.116	0.74978
	20.02	1030	10^{-6}	0.134	0.75035
	25.58	1070	10^{-6}	0.166	0.75046
Rod	30.02	1110	10^{-6}	0.202	0.75010
	35.59	1150	10^{-6}	0.260	0.75058
	40.03	1200	10^{-6}	0.310	0.75020
	45.60	1260	10^{-6}	0.384	0.75054
	50.04	1310	10^{-6}	0.442	0.75092
	10	510	10^{-6}	0.630	0.75143
	15	510	10^{-6}	0.626	0.75164
	20	510	10^{-6}	0.620	0.75119
	25	510	10^{-6}	0.612	0.75208
Sphere	30	510	10^{-6}	0.606	0.75178
	35	510	10^{-6}	0.598	0.75136
	40	510	10^{-6}	0.598	0.75189
	45	520	10^{-6}	0.600	0.75189
	50	520	10^{-6}	0.606	0.75107

Table 6. *Cont.*

AuNP Type	r_{eff}(nm)	λ_{max}(nm)	f_v	P_l(W)	Effective Apoptosis Ratio
Shell	9.96	530	10^{-6}	0.458	0.75111
	15.16	560	10^{-6}	0.360	0.75065
	20.11	590	10^{-6}	0.284	0.75089
	24.97	630	10^{-6}	0.248	0.74977
	30.03	650	10^{-6}	0.284	0.75083
	35.09	630	10^{-6}	0.302	0.75042
	39.99	860	10^{-6}	0.338	0.75095
	44.95	720	10^{-6}	0.466	0.75094
	49.98	720	10^{-6}	0.416	0.75081
Pyramid	10.04	590	10^{-6}	0.430	0.75065
	15.06	590	10^{-6}	0.426	0.75119
	20.07	600	10^{-6}	0.420	0.75090
	24.94	600	10^{-6}	0.418	0.75056
	29.96	610	10^{-6}	0.418	0.75072
	34.98	620	10^{-6}	0.424	0.75143
	40.15	630	10^{-6}	0.434	0.75101
	45.01	640	10^{-6}	0.454	0.75066
	49.88	650	10^{-6}	0.480	0.75088
Prism	10.02	530	10^{-6}	0.564	0.75141
	15.02	530	10^{-6}	0.562	0.75164
	20.03	530	10^{-6}	0.558	0.75132
	25.04	530	10^{-6}	0.556	0.75146
	30.05	540	10^{-6}	0.554	0.75149
	35.06	540	10^{-6}	0.552	0.75140
	40.06	540	10^{-6}	0.554	0.75114
	45.07	550	10^{-6}	0.558	0.75140
	50.08	550	10^{-6}	0.560	0.75141
Cube	9.93	530	10^{-6}	0.518	0.75119
	14.89	530	10^{-6}	0.510	0.75101
	19.85	530	10^{-6}	0.502	0.75101
	25.12	530	10^{-6}	0.494	0.75104
	30.09	530	10^{-6}	0.490	0.75104
	35.05	530	10^{-6}	0.492	0.75148
	40.01	540	10^{-6}	0.496	0.75088
	44.98	540	10^{-6}	0.512	0.75102
	49.94	540	10^{-6}	0.534	0.75131

4. Conclusions

In this study, a numerical study based on heat transfer theory was performed to investigate photothermal therapy using AuNPs on an actual skin layer containing squamous cell carcinoma. The temperature distribution inside the biological tissue was calculated using the Pennes bioheat equation, and the optical properties of the AuNPs were calculated using the discrete dipole approximation method.

The optimal treatment conditions for photothermal therapy were confirmed through the apoptosis ratio, which quantitatively confirms the volume ratio corresponding to the temperature band of apoptosis in tumors, the thermal hazard value that confirms the thermal damage of surrounding normal tissues, and the effective apoptosis ratio that considers the above two variables at the same time.

Finally, the AuNP shape, r_{eff}, f_v, λ_{max}, and P_l that afforded the optimal therapeutic effect were obtained; hence, they can be utilized as the optimal treatment conditions for performing photothermal treatment in the future. In addition, future studies will not simply assume a cylindrical tumor, but rather conduct studies on tumors of various shapes.

Author Contributions: Conceptualization, D.K. and H.K.; Data curation, D.K.; Formal analysis, D.K.; Funding acquisition, H.K.; Investigation, D.K.; Methodology, D.K.; Project administration, H.K.; Resources, H.K.; Software, D.K.; Supervision, H.K.; Validation, D.K.; Visualization, D.K.; Writing—original draft, D.K.; Writing—review and editing, H.K. All authors have read and agreed to the published version of the manuscript.

Institutional Review Board Statement: Not applicable.

Informed Consent Statement: Not applicable.

Data Availability Statement: Data sharing is not applicable to this article.

Conflicts of Interest: The authors declare that they have no known competing financial interests or personal relationships that could have influenced the work reported herein.

Abbreviations

The following abbreviations are used herein:

C	Cross-section area (m^2)
c_p	Heat capacity (J/kgK)
d	Thickness (m)
E	Electric field (N/C)
f_v	Volume fraction of AuNPs
g	Anisotropy factor
k	Wavenumber of radiation (1/m)
k_m	Thermal conductivity (W/mK)
P	Polarization vector (C/m^2)
P_l	Intensity of laser (W)
q	Volumetric heat source (W/m^3)
Q	Dimensionless efficiency factor
r	Position vector
r_{eff}	Effective radius of particle (m)
t	Time (s)
T	Temperature (K)
V	Volume (m^3)
w	Weight
Greek symbols	
α	Polarizability (C^{2}m^2/J)
θ_A	Apoptosis ratio
θ_H	Thermal hazard value
θ_{eff}	Effective apoptosis ratio
λ	Wavelength (m)
μ	Optical coefficient (1/m)
μ'	Reduced optical coefficient (1/m)
ρ	Density (kg/m^3)
Subscripts	
abs	Absorption
b	Blood
ext	Extinction
l	Laser
m	Medium
max	Maximum
met	Metabolic
n	Nano particle
sca	Scattering
tot	Total
x, y, z	Notation of direction
Superscripts	
$*$	Complex conjugate

References

1. Skaggs, R.; Coldiron, B. Skin biopsy and skin cancer treatment use in the Medicare population, 1993 to 2016. *J. Am. Acad. Dermatol.* **2021**, *84*, 53–59. [CrossRef] [PubMed]
2. Wei, L.; Christensen, S.R.; Fitzgerald, M.E.; Graham, J.; Hutson, N.D.; Zhang, C.; Huang, Z.; Hu, Q.; Zhan, F.; Xie, J. Ultradeep sequencing differentiates patterns of skin clonal mutations associated with sun-exposure status and skin cancer burden. *Sci. Adv.* **2021**, *7*, eabd7703. [CrossRef] [PubMed]

3. Donati, D.; Brown, S.; Eu, K.; Ho, Y.; Seow-Choen, F. Comparison between midline incision and limited right skin crease incision for right-sided colonic cancers. *Tech. Coloproctology* **2002**, *6*, 1–4. [CrossRef] [PubMed]
4. Holt, P. Cryotherapy for skin cancer: Results over a 5-year period using liquid nitrogen spray cryosurgery. *Br. J. Dermatol.* **1988**, *119*, 231–240. [CrossRef] [PubMed]
5. Kirby, J.S.; Miller, C.J. Intralesional chemotherapy for nonmelanoma skin cancer: A practical review. *J. Am. Acad. Dermatol.* **2010**, *63*, 689–702. [CrossRef]
6. Di Franco, R.; Sammarco, E.; Calvanese, M.G.; De Natale, F.; Falivene, S.; DiLecce, A.; Giugliano, F.M.; Murino, P.; Manzo, R.; Cappabianca, S. Preventing the acute skin side effects in patients treated with radiotherapy for breast cancer: The use of corneometry in order to evaluate the protective effect of moisturizing creams. *Radiat. Oncol.* **2013**, *8*, 1–7. [CrossRef]
7. Kwikkel, H.; Helmerhorst, T.J.; Bezemer, P.; Quaak, M.; Stolk, J. Laser or cryotherapy for cervical intraepithelial neoplasia: A randomized study to compare efficacy and side effects. *Gynecol. Oncol.* **1985**, *22*, 23–31. [CrossRef]
8. Pearce, A.; Haas, M.; Viney, R.; Pearson, S.-A.; Haywood, P.; Brown, C.; Ward, R. Incidence and severity of self-reported chemotherapy side effects in routine care: A prospective cohort study. *PLoS ONE* **2017**, *12*, e0184360. [CrossRef]
9. Johnson, C.; Serpell, J. Wound infection after abdominal incision with scalpel or diathermy. *Scalpel* **1990**, *130*, 18–95. [CrossRef]
10. Lerner, S.F. Small incision trabeculectomy avoiding Tenon's capsule: A new procedure for glaucoma surgery. *Ophthalmology* **1997**, *104*, 1237–1241. [CrossRef]
11. Huang, X.; El-Sayed, M.A. Plasmonic photo-thermal therapy (PPTT). *Alex. J. Med.* **2011**, *47*, 1–9. [CrossRef]
12. Robinson, J.T.; Tabakman, S.M.; Liang, Y.; Wang, H.; Sanchez Casalongue, H.; Vinh, D.; Dai, H. Ultrasmall reduced graphene oxide with high near-infrared absorbance for photothermal therapy. *J. Am. Chem. Soc.* **2011**, *133*, 6825–6831. [CrossRef] [PubMed]
13. Gurevich, Y.; Logvinov, G.; Lashkevich, I. Effective thermal conductivity: Application to photothermal experiments for the case of bulk light absorption. *Phys. Status Solidi (B)* **2004**, *241*, 1286–1298. [CrossRef]
14. Aamodt, L.; Murphy, J. Thermal effects in photothermal spectroscopy and photothermal imaging. *J. Appl. Phys.* **1983**, *54*, 581–591. [CrossRef]
15. Espinosa, A.; Di Corato, R.; Kolosnjaj-Tabi, J.; Flaud, P.; Pellegrino, T.; Wilhelm, C. Duality of iron oxide nanoparticles in cancer therapy: Amplification of heating efficiency by magnetic hyperthermia and photothermal bimodal treatment. *ACS Nano* **2016**, *10*, 2436–2446. [CrossRef]
16. Abbas, M.; Zou, Q.; Li, S.; Yan, X. Self-assembled peptide-and protein-based nanomaterials for antitumor photodynamic and photothermal therapy. *Adv. Mater.* **2017**, *29*, 1605021. [CrossRef]
17. Huang, X.; El-Sayed, M.A. Gold nanoparticles: Optical properties and implementations in cancer diagnosis and photothermal therapy. *J. Adv. Res.* **2010**, *1*, 13–28. [CrossRef]
18. Salcman, M.; Samaras, G.M. Interstitial microwave hyperthermia for brain tumors. *J. Neuro-Oncol.* **1983**, *1*, 225–236. [CrossRef]
19. Meglinski, I.V.; Matcher, S.J. Quantitative assessment of skin layers absorption and skin reflectance spectra simulation in the visible and near-infrared spectral regions. *Physiol. Meas.* **2002**, *23*, 741. [CrossRef]
20. Khlebtsov, B.; Zharov, V.; Melnikov, A.; Tuchin, V.; Khlebtsov, N. Optical amplification of photothermal therapy with gold nanoparticles and nanoclusters. *Nanotechnology* **2006**, *17*, 5167. [CrossRef]
21. Hwang, S.; Nam, J.; Jung, S.; Song, J.; Doh, H.; Kim, S. Gold nanoparticle-mediated photothermal therapy: Current status and future perspective. *Nanomedicine* **2014**, *9*, 2003–2022. [CrossRef] [PubMed]
22. Li, J.-L.; Gu, M. Gold-nanoparticle-enhanced cancer photothermal therapy. *IEEE J. Sel. Top. Quantum Electron.* **2009**, *16*, 989–996.
23. El-Sayed, I.H.; Huang, X.; El-Sayed, M.A. Selective laser photo-thermal therapy of epithelial carcinoma using anti-EGFR antibody conjugated gold nanoparticles. *Cancer Lett.* **2006**, *239*, 129–135. [CrossRef] [PubMed]
24. Singh, M.; Harris-Birtill, D.C.; Markar, S.R.; Hanna, G.B.; Elson, D.S. Application of gold nanoparticles for gastrointestinal cancer theranostics: A systematic review. *Nanomed. Nanotechnol. Biol. Med.* **2015**, *11*, 2083–2098. [CrossRef] [PubMed]
25. D'Acunto, M.; Cioni, P.; Gabellieri, E.; Presciuttini, G. Exploiting gold nanoparticles for diagnosis and cancer treatments. *Nanotechnology* **2021**, *32*, 192001. [CrossRef]
26. Bucharskaya, A.B.; Maslyakova, G.; Dikht, N.; Navolokin, N.; Terentyuk, G.; Bashkatov, A.; Genina, E.; Khlebtsov, B.; Khlebtsov, N.; Tuchin, V. Plasmonic photothermal therapy of transplanted tumors in rats at multiple intravenous injection of gold nanorods. *BioNanoScience* **2017**, *7*, 216–221. [CrossRef]
27. Wyllie, A.H. Cell death. *Cytol. Cell Physiol.* **1987**, 755–785. [CrossRef]
28. Song, A.S.; Najjar, A.M.; Diller, K.R. Thermally induced apoptosis, necrosis, and heat shock protein expression in three-dimensional culture. *J. Biomech. Eng.* **2014**, *136*, 071006. [CrossRef]
29. Zhu, X.; Feng, W.; Chang, J.; Tan, Y.-W.; Li, J.; Chen, M.; Sun, Y.; Li, F. Temperature-feedback upconversion nanocomposite for accurate photothermal therapy at facile temperature. *Nat. Commun.* **2016**, *7*, 1–10. [CrossRef]
30. Nam, J.; Son, S.; Ochyl, L.J.; Kuai, R.; Schwendeman, A.; Moon, J.J. Chemo-photothermal therapy combination elicits anti-tumor immunity against advanced metastatic cancer. *Nat. Commun.* **2018**, *9*, 1–13. [CrossRef]
31. Mackey, M.A.; Ali, M.R.; Austin, L.A.; Near, R.D.; El-Sayed, M.A. The most effective gold nanorod size for plasmonic photothermal therapy: Theory and in vitro experiments. *J. Phys. Chem. B* **2014**, *118*, 1319–1326. [CrossRef] [PubMed]
32. Van de Broek, B.; Devoogdt, N.; D'Hollander, A.; Gijs, H.-L.; Jans, K.; Lagae, L.; Muyldermans, S.; Maes, G.; Borghs, G. Specific cell targeting with nanobody conjugated branched gold nanoparticles for photothermal therapy. *ACS Nano* **2011**, *5*, 4319–4328. [CrossRef] [PubMed]

33. Xi, D.; Xiao, M.; Cao, J.; Zhao, L.; Xu, N.; Long, S.; Fan, J.; Shao, K.; Sun, W.; Yan, X. NIR light-driving barrier-free group rotation in nanoparticles with an 88.3% photothermal conversion efficiency for photothermal therapy. *Adv. Mater.* **2020**, *32*, 1907855. [CrossRef] [PubMed]

34. Kim, M.; Kim, G.; Kim, D.; Yoo, J.; Kim, D.-K.; Kim, H. Numerical study on effective conditions for the induction of apoptotic temperatures for various tumor aspect ratios using a single continuous-wave laser in photothermal therapy using gold nanorods. *Cancers* **2019**, *11*, 764. [CrossRef]

35. Draine, B.T.; Flatau, P.J. Discrete-dipole approximation for periodic targets: Theory and tests. *Josa A* **2008**, *25*, 2693–2703. [CrossRef]

36. Draine, B.T.; Flatau, P.J. Discrete-dipole approximation for scattering calculations. *Josa A* **1994**, *11*, 1491–1499. [CrossRef]

37. Mie, G. Beiträge zur Optik trüber Medien, speziell kolloidaler Metallösungen. *Ann. Phys.* **1908**, *330*, 377–445. [CrossRef]

38. Mie, G. Contributions to the optics of turbid media, particularly of colloidal metal solutions. *Contrib. Opt. Turbid Media* **1976**, *25*, 377–445.

39. Yurkin, M.A.; Hoekstra, A.G.; Brock, R.S.; Lu, J.Q. Systematic comparison of the discrete dipole approximation and the finite difference time domain method for large dielectric scatterers. *Opt. Express* **2007**, *15*, 17902–17911. [CrossRef]

40. Pennes, H.H. Analysis of tissue and arterial blood temperatures in the resting human forearm. *J. Appl. Physiol.* **1948**, *1*, 93–122. [CrossRef]

41. Chang, W.-S.; Na, S.-J. A study on heat source equations for the prediction of weld shape and thermal deformation in laser microwelding. *Metall. Mater. Trans. B* **2002**, *33*, 757–764. [CrossRef]

42. Dombrovsky, L.A.; Timchenko, V.; Jackson, M.; Yeoh, G.H. A combined transient thermal model for laser hyperthermia of tumors with embedded gold nanoshells. *Int. J. Heat Mass Transf.* **2011**, *54*, 5459–5469. [CrossRef]

43. Vera, J.; Bayazitoglu, Y. Gold nanoshell density variation with laser power for induced hyperthermia. *Int. J. Heat Mass Transf.* **2009**, *52*, 564–573. [CrossRef]

44. Kim, D.; Kang, S.; Kim, H. Numerical Study on Factors Affecting the Induction of Apoptotic Temperatures of Tumor in the Multi-Layer Skin Structure Using Monte Carlo Method. *Appl. Sci.* **2021**, *11*, 1103. [CrossRef]

45. Jawad, M.M.; Qader, S.T.A.; Zaidan, A.; Zaidan, B.; Naji, A.; Qader, I.T.A. An overview of laser principle, laser-tissue interaction mechanisms and laser safety precautions for medical laser users. *Int. J. Pharmacol.* **2011**, *7*, 149–160. [CrossRef]

46. Soni, S.; Tyagi, H.; Taylor, R.A.; Kumar, A. Investigation on nanoparticle distribution for thermal ablation of a tumour subjected to nanoparticle assisted thermal therapy. *J. Therm. Biol.* **2014**, *43*, 70–80. [CrossRef]

47. Ren, Y.; Qi, H.; Chen, Q.; Ruan, L. Thermal dosage investigation for optimal temperature distribution in gold nanoparticle enhanced photothermal therapy. *Int. J. Heat Mass Transf.* **2017**, *106*, 212–221. [CrossRef]

48. Salomatina, E.V.; Jiang, B.; Novak, J.; Yaroslavsky, A.N. Optical properties of normal and cancerous human skin in the visible and near-infrared spectral range. *J. Biomed. Opt.* **2006**, *11*, 064026. [CrossRef]

49. Çetingül, M.P.; Herman, C. A heat transfer model of skin tissue for the detection of lesions: Sensitivity analysis. *Phys. Med. Biol.* **2010**, *55*, 5933. [CrossRef]

50. Çetingül, M.P.; Herman, C. Quantification of the thermal signature of a melanoma lesion. *Int. J. Therm. Sci.* **2011**, *50*, 421–431. [CrossRef]

51. Jiang, S.; Ma, N.; Li, H.; Zhang, X. Effects of thermal properties and geometrical dimensions on skin burn injuries. *Burns* **2002**, *28*, 713–717. [CrossRef]

52. Torvi, D.; Dale, J. A finite element model of skin subjected to a flash fire. *J. Biomech. Eng.* **1994**, *116*, 250–255. [CrossRef] [PubMed]

53. Wilson, S.B.; Spence, V.A. A tissue heat transfer model for relating dynamic skin temperature changes to physiological parameters. *Phys. Med. Biol.* **1988**, *33*, 895. [CrossRef] [PubMed]

54. Prasad, B.; Kim, S.; Cho, W.; Kim, S.; Kim, J.K. Effect of tumor properties on energy absorption, temperature mapping, and thermal dose in 13.56-MHz radiofrequency hyperthermia. *J. Therm. Biol.* **2018**, *74*, 281–289. [CrossRef] [PubMed]